

## Influence of pinholes and weak-points in aluminum-oxide Josephson junctions

K. Bayros , M. J. Cyster , J. S. Smith , and J. H. Cole \*

*Chemical and Quantum Physics, School of Science, RMIT University, Melbourne, Victoria 3001, Australia*

 (Received 27 November 2023; revised 29 February 2024; accepted 22 March 2024; published 10 April 2024)

Josephson junctions are the key components used in superconducting qubits for quantum computing. The advancement of quantum computing is limited by a lack of stability and reproducibility of qubits, which ultimately originates in the amorphous tunnel barrier of the Josephson junctions and other material imperfections. Pinholes in the junction have been suggested as one of the possible contributors to these instabilities, but evidence of their existence and the effect they might have on transport is unclear. We use molecular dynamics to create three-dimensional atomistic models to describe Al-AIO<sub>x</sub>-Al tunnel junctions, showing that pinholes form when oxidation of the barrier is incomplete. Following this, we use the atomistic model and simulate the electronic transport properties for tunnel junctions with different barrier thicknesses using the nonequilibrium Green's function formalism. We observe that pinholes may contribute to excess quasiparticle current flow in Al-AIO<sub>x</sub>-Al tunnel junctions with thinner barriers, and in thicker barriers we observe weak-points that facilitate leakage currents even when the oxide is continuous. We find that the disordered nature of the amorphous barrier results in significant variations in the transport properties. Additionally, we determine the current-phase relationship for our atomistic structures, confirming that devices with pinholes and weak-points cause a deviation from the ideal sinusoidal Josephson relationship.

DOI: [10.1103/PhysRevMaterials.8.046202](https://doi.org/10.1103/PhysRevMaterials.8.046202)

### I. INTRODUCTION

Josephson junctions are one of the key components used in superconducting qubits for quantum computers [1–3]. While there have been significant developments in the fabrication processes of Josephson junctions, which now enable us to have working examples of small-scale quantum computing [4–6], we still see significant problems with device stability and reproducibility. In particular, large variabilities have been found in the coherence times with time [7,8], and across different qubits on a quantum computing chip [9–11]. Variations have also been found in the critical currents between Josephson junctions fabricated in the same way [12]. These variations in the qubit parameters mean that significant tuning is required to ensure that qubits across the chip function similarly. Although qubits can be tuned [13,14], this typically requires more gates to be patterned onto quantum computing chips, as well as recalibration during the computation [6,15]. This significantly limits the reliability of quantum computing chips that are fabricated today. It is not yet clear what causes stability and reproducibility problems in these devices, however a large amount of research discusses the importance of the tunnel barrier in this context [16]. Often comprised of an amorphous metal-oxide material, the tunnel barrier is inherently disordered, inviting the possibility of structures that could act as two-level systems that couple to the qubit current causing instabilities in its parameters. A particular type of imperfection in the tunnel barrier that has been proposed are microscopic metallic links, coined “pinholes.” These pinholes may increase the current that couples to two-level systems in the barrier, exacerbating instabilities [17].

In the literature there is currently conflicting evidence on the role and prevalence of pinholes. Zhou *et al.* [18] find that pinholes may exist in particular circumstances, such as when the oxide barrier is too thin, whereas Greibe *et al.* [19] develop a model that rules out pinholes as the source of excess current. On the other hand, Tolpygo *et al.* [20] show that pinholes may not exist in a newly fabricated device, however they may form through degradation of the oxide when the junction is used in a circuit. Recent work has studied the effect of Josephson harmonics on the current-phase relationship (CPR), highlighting that the disordered nature of the oxide barrier could contribute to effects in the CPR, specifically if there are high transmission channels present [21].

This paper uses computational techniques to study how pinholes form, and it aims to investigate what effects they might have on transport properties in Josephson junction devices that are fabricated today. Commonly, Josephson junctions are fabricated as Al-AIO<sub>x</sub>-Al tunnel junctions [22–24]. This study investigates pinhole formation during AIO<sub>x</sub> growth to discuss under which conditions they might be stable, and what effect stable pinholes might have on electronic transport through the device. We begin by discussing the stability of pinholes following Zhou *et al.* [18], who model a cylindrical pinhole in an otherwise uniform oxide barrier. Using the interfacial surface energies between materials in the system, the stability of pinholes can be determined. Using a similar method, we determine the stability of cylindrical pinholes with increasing radii for different barrier thicknesses. Using the same geometries, we then calculate the transport properties for each of these devices.

To then investigate the formation and closing of pinholes more realistically, we use our previously developed molecular-dynamics approach [25] to grow Al-AIO<sub>x</sub>-Al

\*jared.cole@rmit.edu.au

tunnel junctions with different amounts of oxide in the barrier.

Using a tight-binding description of the system, we employ a nonequilibrium Green's function (NEGF) approach to investigate normal (single-electron) transport in the structures studied herein. NEGF is a numerical approach that has been widely used for calculating transport properties in nanoscale devices [26], and it has also been used explicitly for the case of Al-AIO<sub>x</sub>-Al tunnel junctions [27]. In this work, we determine the transmission, resistance-area, and current density through full three-dimensional models of Al-AIO<sub>x</sub>-Al tunnel junctions with different amounts of oxide. Understanding variations in the normal transport based on structural irregularities can suggest causes for variation in the superconducting properties.

To understand how the normal transport translates to the superconducting (correlated-electron) transport, the Ambegaokaar-Baratoff (AB) relation is commonly used [28,29]. It specifically relates normal-state resistance to the superconducting critical current. The validity of this relationship is unclear when there are pinholes present in the oxide barrier. As an alternative, the model in this work is used to calculate the transmission eigenvalues for each of our structures, which in turn allows us to determine the contributions from different transmission channels and the effects they have on the CPR.

From a toy model we determine that pinholes may be present in thinner barriers and a source of single-electron current. We then use the analysis from the toy model to understand the transport properties of a three-dimensional atomistic model describing Al-AIO<sub>x</sub>-Al tunnel junctions derived from molecular-dynamics simulations. Our results show that there is a significant amount of variability in the transport properties. These variabilities are still present for devices without pinholes, indicating that the variation is a product of the inherently disordered AIO<sub>x</sub> barrier. We also find that the amorphous structure of the oxide results in a nonuniform electric potential, which makes the metal-insulator transition of the barrier less clear compared to analysis from our toy model. Specifically, some results highlight that thick barriers with no pinholes may remain conductive. These devices do not have clear pinholes in the barrier, but they have weak-points that can facilitate single-electron current flow. This could indicate a situation in which a seemingly complete barrier could result in a dysfunctional device.

## II. TOY MODEL

Given the complex structure of disordered AIO<sub>x</sub>, we first develop an idealized model to understand how pinholes of a simple structure remain stable in the barrier and also how systematic changes in pinhole size may affect the transport properties of tunnel junctions. For this section, we use a geometric model with pinholes described as cylinders in an otherwise uniform oxide layer in Al-AIO<sub>x</sub>-Al tunnel junctions. Figure 1 schematically depicts the geometry of our model.

### A. Stability of pinholes

To study under which conditions pinholes are stable in the oxide barrier, we follow methods outlined in Zhou *et al.*

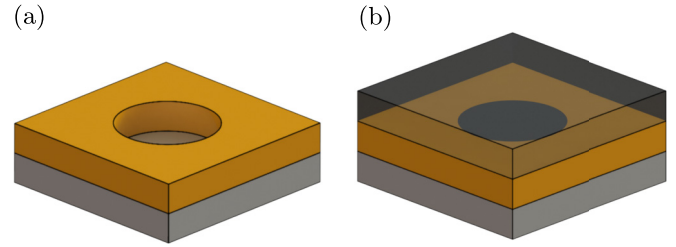


FIG. 1. A schematic representation of a simple cylindrical pinhole in an Al-AIO<sub>x</sub>-Al tunnel junction. (a) Aluminum bottom contact (gray) and an aluminum-oxide layer (orange) with a pinhole. (b) A complete tunnel junction showing the aluminum-oxide layer with a pinhole underneath an aluminum top contact (transparent gray).

[18] to determine the interfacial surface energies between different materials in our system. Previous theoretical studies use molecular-dynamics methods to calculate the interfacial surface energies for different Al and AIO<sub>x</sub> interfaces [30], finding  $\gamma_{\text{Al}} = 0.057 \text{ eV}/\text{\AA}^2$ ,  $\gamma_{\text{AlO}} = 0.341 \text{ eV}/\text{\AA}^2$ , and  $\gamma_{\text{Al/AIO}} = 0.186 \text{ eV}/\text{\AA}^2$ , which we use in subsequent calculations. The surface energy,  $\gamma$ , is between the materials specified in the subscript, and where only one material is given, the interface is vacuum.

Equation (1) describes the hole formation energy for the geometry shown in Fig. 1(a), with a pinhole in the oxide on an Al bottom contact and vacuum above the oxide (before the top contact is deposited),

$$\Delta E = \pi r^2(\gamma_{\text{Al}} - \gamma_{\text{AlO}} - \gamma_{\text{Al/AIO}}) + 2\pi rh(\gamma_{\text{AlO}}). \quad (1)$$

A similar equation can be derived for the case with an Al top contact deposited. Using Eq. (1), we can determine the energy required to form holes of different radii,  $r$ , in the oxide barrier at different thicknesses,  $h$ . Figure 2 shows this relationship for the two geometries shown in Fig. 1.

A negative hole formation energy implies that for a uniform oxide layer arrangement it is more energetically favorable to have pinholes and they may form spontaneously. On the other hand, a positive hole formation energy indicates that energy is required to form pinholes in a uniform oxide layer. The results in Fig. 2 show that for thinner oxides, it is more energetically favorable for larger pinholes to form. However, as the oxide is grown thicker there is a crossover point where it becomes more energetically favorable to form smaller pinholes. This is consistent with the oxide beginning to cover more of the underlying substrate, resulting in the formation of smaller holes. Although this is the case, it is more common that the formation energy becomes positive before we see this cross over, indicating it is not favorable for pinholes of any size to form.

For the case of a complete junction as depicted in Fig. 1(b), where aluminum is deposited as a top contact, we find that the formation energy remains negative for larger oxide thicknesses. This implies that thicker oxide barriers are required to prevent the spontaneous formation of pinholes compared to the case when the oxide is exposed to vacuum. Consequently, this means that the deposition of aluminum on top of existing pinholes may increase their stability.

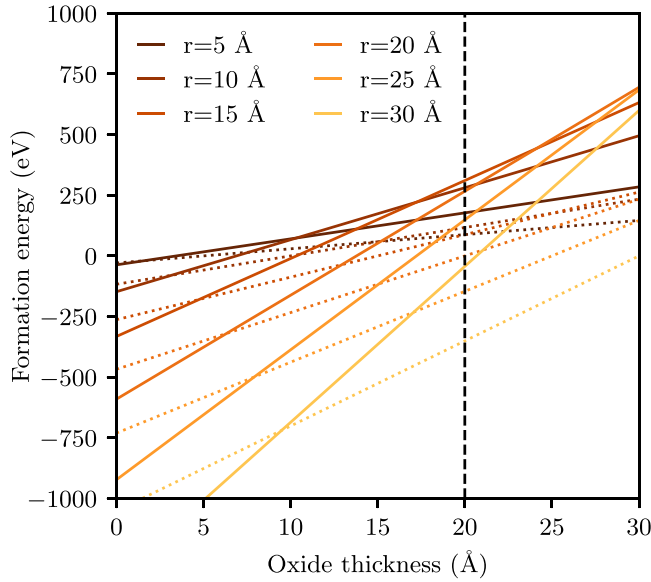


FIG. 2. The energy required to form cylindrical pinholes with different radii in  $\text{AlO}_x$  barriers of different thicknesses. Solid lines indicate a calculation with vacuum above the oxide layer, while dashed lines show a calculation with an aluminum top contact. The black dashed line indicates a typical oxide thickness of 20 Å used in Al- $\text{AlO}_x$ -Al junctions.

The results in Fig. 2 are consistent with previous findings in work on dewetting of thin-films in which it was found that the number of holes formed scales inversely with the film thickness [31]. This highlights the importance of considering the stability of pinholes when studying the formation of Al- $\text{AlO}_x$ -Al tunnel junctions, specifically ones with thinner barriers.

### B. Normal transport in a toy model

Using a model with the same geometry as depicted in Fig. 1(b), we develop a three-dimensional tight-binding model. We do this here to compare to later sections where this method is used with a full atomistic description of the device (see Sec. IV). For all our calculations, we take  $z$  to be the direction of transport, so that the  $x$ - $y$  plane defines the cross-sectional area of the device. We define a potential in three dimensions with dimensions in  $x$  and  $y$  of 24 Å × 24 Å, and a barrier height and length of 1.3 eV and 30 Å, respectively. When Al- $\text{AlO}_x$ -Al junctions are fabricated, they can range from 0.03 to 1  $\mu\text{m}^2$  in cross-sectional area [32,33], which is significantly larger than our simulated device area. To account for this, we apply periodic boundary conditions in  $x$  and  $y$ , whereas  $z$  has open boundary conditions to simulate transport [27].

To calculate the normal transport through the junction, we employ a nonequilibrium Green's function (NEGF) approach, which is a widely used method for solving the time-independent Schrödinger equation (TISE) numerically for a system with open boundary conditions [26,34]. This allows us to simulate the effects of attaching a source and drain contact to the barrier and subsequently calculate properties

such as the transmission and normal state resistance through the device.

The retarded Green's function is given by

$$G^r(E) = [(E + i\eta)I - H - \Sigma_S - \Sigma_D]^{-1}, \quad (2)$$

where  $I$  is the identity matrix, and  $i\eta$  is a positive imaginary infinitesimal number.

The Hamiltonian,  $H = T + U$ , is defined with a kinetic,  $T$ , and potential,  $U$ , energy operator. We describe our system using a second-order finite-difference representation of the kinetic energy operator,

$$T = \sum_i^N \varepsilon |i\rangle \langle i| - \sum_{\langle i,j \rangle}^N t_k |i\rangle \langle j|, \quad (3)$$

where  $\varepsilon = 2t_x + 2t_y + 2t_z$ , and  $k \in \{x, y, z\}$ . The hopping parameter,  $t_k$ , is given by  $t_k = \frac{\hbar^2}{2m^*a_k^2}$ , where  $m^*$  is the effective mass and  $a_k$  is the finite grid spacing in a given direction. We assume the effective electron mass  $m^* = 9.1 \times 10^{-31}$  kg as the structures considered are mostly pure aluminum and we use  $a_k = 1/3$  Å throughout as this has previously shown good convergence for these structures [27]. In this section, the electrostatic potential energy term,  $U$ , is applied as a rectangular barrier with a cylindrical hole in it. In Sec. III,  $U$  is determined from the charges and positions of the atoms. The self-energies for the source and drain,  $\Sigma_{S/D}$ , are calculated recursively [35], and these terms account for the effect of attaching semi-infinite leads.

The normal transmission is then calculated from [26]

$$T(E) = \text{Tr}(\Gamma_S G^r \Gamma_D G^a), \quad (4)$$

where the broadening matrices are given by  $\Gamma_{S,D} = i(\Sigma_{S,D} - \Sigma_{S,D}^\dagger)$ , and the advanced Green's function is  $G^a = G^{r\dagger}$ .

The Landauer-Büttiker formula allows us to use  $T(E)$  to calculate the current in a device:

$$I = \frac{2e^2}{h} \int_{-\infty}^{\infty} T(E) [f_S(E) - f_D(E)] dE, \quad (5)$$

where the Fermi-Dirac distributions for the source and drain contacts are given by  $f_{S,D} = 1/[\exp((E - E_F - eV_{S,D})/2)/k_B T) + 1]$ ,  $e$  is the electron charge,  $h$  is Planck's constant,  $E_F$  is the Fermi energy,  $k_B$  is the Boltzmann constant, and  $T$  is the temperature.

The normal state resistance at a given energy is determined by taking the zero-temperature, zero-bias limit of Eq. (5) and is given by

$$R_N = \frac{h}{2e^2} \frac{1}{T(E = E_F)}. \quad (6)$$

In general, modeling superconductivity with a NEGF method is more difficult than for normal transport [34,36]. However, we are able to perform an analysis of the transmission channels and thereby estimate the superconducting response in Sec. II C.

Figure 3 shows the transmission and resistance-area product through junctions with pinholes of different radii. To ensure consistency and clarity in later sections, we henceforth define the presence of pinholes using the percentage of

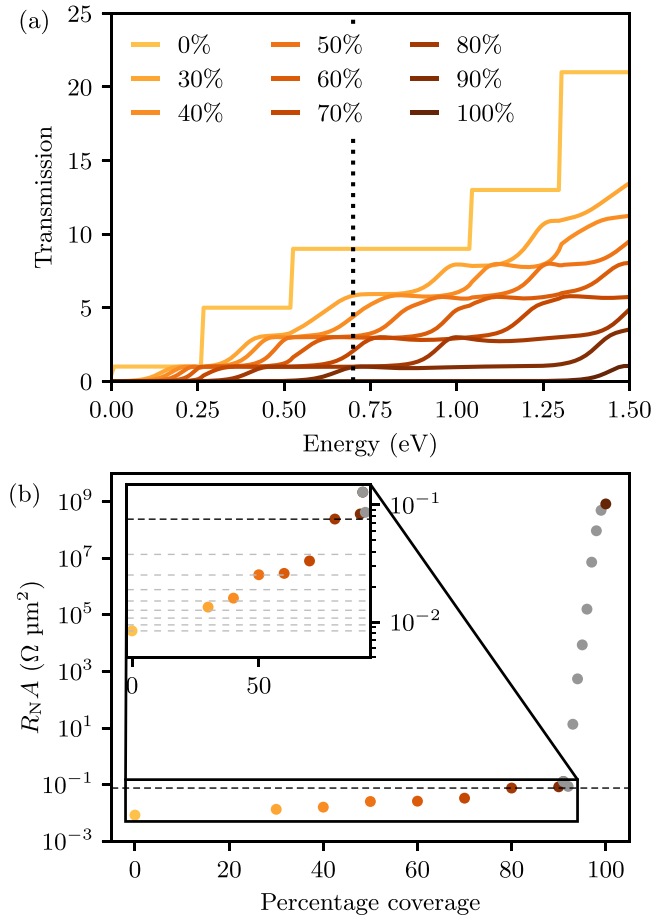


FIG. 3. (a) Transmission through cylindrical pinholes in a 3D rectangular barrier which leave different percentages of the underlying substrate covered, 0%, and 30–100% in intervals of 10%. The vertical dashed line indicates  $E_F = 0.7$  eV. (b) The corresponding resistance-area products calculated at  $E_F$  for each of these junctions with extra points shown between 90% and 100% to show the metal-to-insulator transition. The inset shows a zoomed-in area indicated by the rectangle, with dashed lines corresponding to resistance quanta.

the underlying substrate that is covered. In this section, we model pinholes as cylinders, so our substrate coverage begins at 30% as this allows a full circle to fit within the square cross-sectional area of the device that is simulated.

The  $x$  and  $y$  dimensions of the potential barrier used for results in Fig. 3 are chosen to compare to an example barrier from molecular-dynamics calculations, which are performed in Sec. III. Similarly, we choose the barrier height and thickness to correspond to the thickest barriers in Sec. III. We define the barrier region as the distance from the first oxygen atom to the last oxygen atom in the structure, and then we find the average height in the middle 50% of the barrier to be 1.3 eV. Integrating the electric potential in the barrier region, we find the barrier area and consequently determine the effective width of the barrier as 30 Å.

In Fig. 3(a) we see quantized transmission steps, which show the modes of conduction available. As more of the underlying substrate is covered and the barrier becomes more complete, we see smoothing of these quantized steps. At the extremes, the 0% coverage data show ballistic conduction, and

the 100% indicate transmission through a uniform rectangular barrier. We also see an increase in the transmission at all energies as the percentage coverage decreases, indicative of a more conductive device as is expected when pinholes are present in a barrier.

To calculate the resistance using Eq. (6), we require the Fermi energy,  $E_F$ , of the leads. To determine a suitable  $E_F$ , we use measurements from prior experiments where the resistance-area product was found to be  $R_{NA} = 600 \Omega \mu\text{m}^2$  [37]. Using this value as a standard, we calculate the corresponding transmission value  $T = 4 \times 10^{-5}$  using Eq. (6) and the quoted device cross-sectional area. Linearly interpolating between points in the transmission function of our 100% coverage data set, we determine the corresponding  $E_F \approx 0.7$  eV, which we use for all subsequent calculations.

Figure 3(b) shows  $R_{NA}$  calculations using  $E_F = 0.7$  eV, marked with a dashed line with the transmission results in Fig. 3(a). Between 90% and 100% coverage, we have included extra points in intervals of 1% to highlight the sharp increase in resistive behavior as we approach 100% coverage. This jump corresponds to the transition from metal conduction to insulating barrier. To demonstrate this clearly, the inset in Fig. 3(b) shows horizontal dashed lines at multiples of one resistance quantum. The darkest dashed line corresponds to  $T = 1$ , or a resistance value of  $R_{NA} = 0.07 \Omega \mu\text{m}^2$ , which is also marked on the main figure for clarity. Beyond this there are no modes to facilitate ballistic conduction, and the device becomes insulating, i.e., all conduction occurs via barrier tunneling.

### C. Superconducting transport in a toy model

The supercurrent-phase relationship [29,38,39] in a Josephson junction is given by

$$I_S(\phi) = \sum_p \frac{e\Delta^2 \tau_p \sin(\phi)}{2\hbar E_+^{\text{ABS}}} \tanh\left[\frac{E_+^{\text{ABS}}(\phi)}{2k_B T}\right], \quad (7)$$

where

$$E_{\pm}^{\text{ABS}} = \pm\Delta\sqrt{1 - \tau_p \sin^2(\phi/2)}. \quad (8)$$

Here,  $\tau_p$  is the transmission probability for a transmission eigenmode  $p$ ,  $\Delta$  is the superconducting order parameter, and  $\hbar$  is the reduced Planck constant.  $E_{\pm}^{\text{ABS}}$  is the energy of the Andreev bound states which mediate Cooper pair transfer between superconducting regions, leading to the Josephson effect. Equation (7) is valid for short Josephson junctions, i.e., when the device length is much less than the superconducting coherence length [28],  $L \ll \xi$ . Aluminum has a long coherence length of  $\xi = 1600$  nm [40], which makes it widely suitable for Josephson junction applications as the device lengths are typically much shorter.

If  $\tau_p$  is low for all transmission eigenmodes ( $\tau_p \ll 1$ ), the supercurrent-phase relationship in Eq. (7) can be written as the Ambegaokaar-Baratoff (AB) relation,

$$I_S R_N = \frac{\pi \Delta \sin(\phi)}{2e} \tanh\left(\frac{\Delta}{2k_B T}\right), \quad (9)$$

where  $R_N = h/[2e^2 \sum_p \tau_p]$ . This equation relates the transport properties of the device in its normal state to properties

of the device in its superconducting state. In a similar manner, in the fully transparent limit where all  $\tau_p = 1$ , Eq. (7) can be written as the Kulik Omel'yanchuk (KO) relation [41], which is given by

$$I_S R_N = \frac{\pi \Delta \sin(\phi/2)}{e} \tanh\left(\frac{\Delta \cos \phi/2}{2k_B T}\right). \quad (10)$$

Taking the zero-temperature limit of Eq. (10),  $T \rightarrow 0$ , we find  $\tanh(\Delta \cos \phi/2/[2k_B T]) \rightarrow \text{sgn}(\cos \phi/2)$ . Typically, the relations in Eqs. (9) and (10) are used for devices with a complete oxide barrier [42], however in the case of devices with pinholes and weak-points there are channels with different transmission probabilities. This results in a combination of channels that display characteristic AB and KO behavior, as well as behavior in between. Summing these channels then causes a deviation from the ideal sinusoidal Josephson relationship.

To determine the transmission probability eigenvalues [43,44] in our model, we find the largest 30 eigenvalues of the transmission matrix,  $\Gamma_S G^r \Gamma_D G^a$ , which is also used in Eq. (4) to determine the normal transmission.

We take the low-temperature limit of Eq. (7) to calculate the supercurrent for each transmission eigenvalue. We use a low-temperature superconducting gap value of  $\Delta = 200 \mu\text{eV}$  as measured for thin films in prior work [45]. Figure 4 shows the sum of the supercurrent from each of these channels, giving the overall CPR.

Figure 4(a) shows the eigenvalues for the transmission matrix for each toy model structure. Notably, we find that the eigenvalues in the 0% coverage structure are all approximately equal to 1. With increasing coverage, some eigenvalues begin to drop closer to zero, indicating channels with lower transmission probabilities are present. For the structure with 100% coverage, there are no channels with transmission probabilities close to 1. In Fig. 4(b) we see that for a complete barrier (100% coverage) we obtain the expected sinusoidal Josephson relationship for ideal Josephson junctions described by the AB relation [Eq. (9)]. In the other extreme for ballistic conduction, or in the fully transparent limit, we obtain a sawtooth relationship that is given by the KO relation [Eq. (10)]. Aside from these extremes, for percentage coverages between 40% and 70%, the current-phase relationship follows the expected trend from sawtooth to sinusoidal for increasing surface coverages.

We find exceptions to this in the very low-coverage and very high-coverage cases, given by the 30%, 80%, and 90% coverage data sets shown in Fig. 4(c). These cases correspond to two different regimes. In the very low-coverage regime indicated by the 30% coverage data set, the diameter of the cylindrical pinhole is approximately equal to the width of the substrate in our simulation. Due to the periodic boundary conditions applied in our model, this creates a pattern that is similar to diamonds of oxide on a metallic substrate, rather than a hole in a uniform oxide layer. This pattern leads to a shape for the CPR that does not fall between the results for 0% and 40% coverage. In the high-coverage cases we approach a limit where we see a single transmission channel that dominates the conduction. In Fig. 4(a) there are multiple eigenmodes with a transmission probability close to 1, however for 80% and 90% there is only one eigenvalue. This is

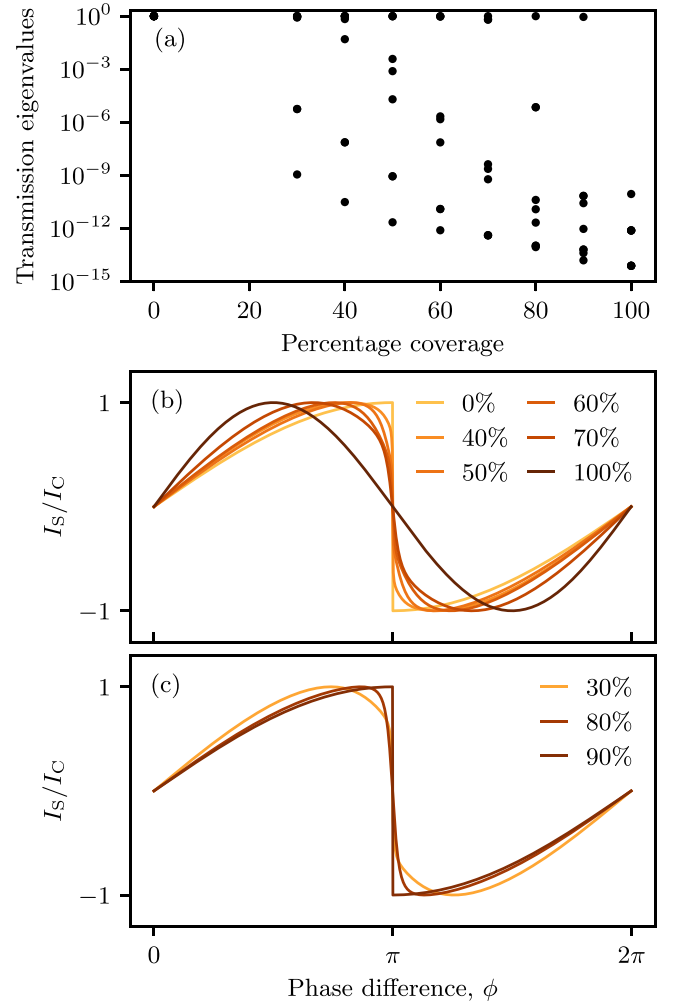


FIG. 4. (a) Eigenvalues of the transmission matrix for the toy model structures 0%, and 30–100 % coverage in 10% intervals. (b) CPRs for structures indicated in the legend. (c) CPRs which correspond to the low and high coverage regimes, for structures indicated in the legend.

resemblant of the Josephson effect for a narrow constriction, or a superconducting quantum point contact [46].

We use the insights from this toy model study to inform our interpretation of results in later sections.

### III. ATOMISTIC MODEL

#### A. Molecular dynamics

In the preceding sections, pinholes have been described as cylindrical holes in the oxide barrier, however in practice pinholes are likely to have irregular shapes. To represent pinhole formation in Al-AlO<sub>x</sub>-Al tunnel junctions more accurately, we use molecular dynamics to grow devices atomistically, allowing us to resolve microscopic structures within the barrier. To simulate this growth, we follow a similar method to that used by Cyster *et al.* [25], and in this work we use the large-scale atomic/molecular massively parallel simulator (LAMMPS) [47,48] to perform our simulations with a ReaxFF force field to describe atom to atom interactions [49,50]. The methods in Cyster *et al.* are designed to replicate the Dolan

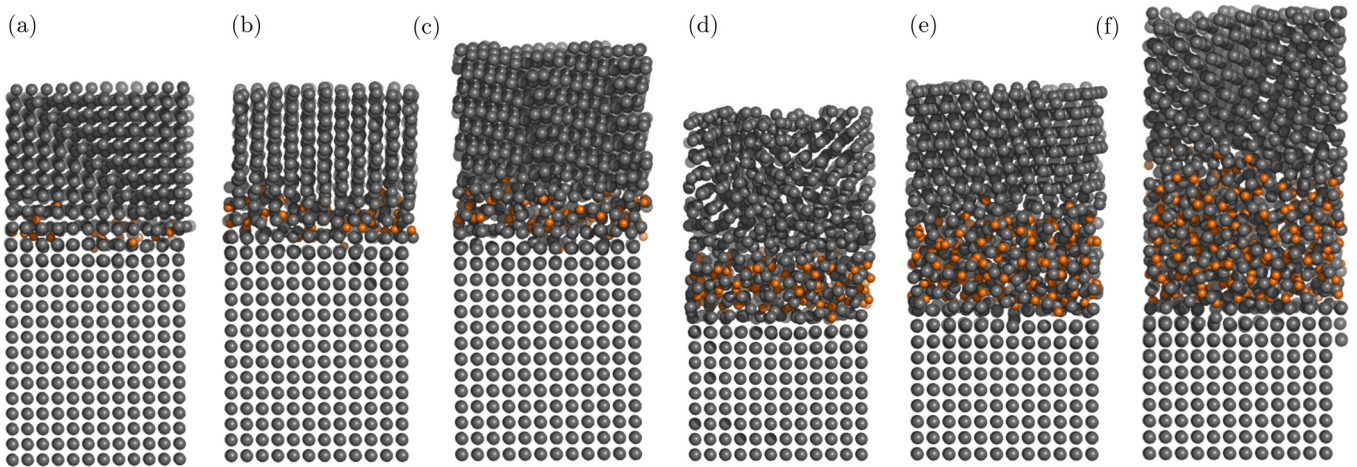


FIG. 5. Molecular-dynamics simulation for a “(100)1” junction with increasing amounts of oxide in the barrier. Aluminum atoms are represented in gray, and oxygen atoms in orange. Structures are presented in order of number of oxygen atoms in the barrier, (a)–(f) no. O = 28, 56, 83, 143, 240, 346. See Table I for more details on oxide thicknesses.

double-angle evaporation process [51], and model the low-pressure oxidation and aluminum evaporation processes that are often used when fabricating Al-AIO<sub>x</sub>-Al tunnel junctions.

Beginning with a 24 Å × 24 Å substrate cell of crystalline aluminum, we introduce a vacuum above the substrate and grow an AIO<sub>x</sub> layer by introducing oxygen atom-by-atom with atom trajectories and velocities sampled from a Boltzmann distribution. We create a set of 12 structures with increasing numbers of oxygen atoms in the AIO<sub>x</sub> layer, some of which are shown in Fig. 5. We find that the layers with less oxide tend to contain pinholes that close over as more oxide is grown (see Sec. III B).

We find that this simulation method results in self-limiting AIO<sub>x</sub> growth when the LAMMPS/ReaxFF force field is used [in contrast to our previous work with GULP/Streitz and Mintmire (SM) [27], which did not self-limit]. However the resulting oxide grown with LAMMPS/ReaxFF is thinner (approximately 1 Å [37,52] than is typically observed experimentally. To study thicker oxides, we replicate the methods used to grow >10-nm-thick oxides experimentally. Namely, after the oxide self-limits, an atomically thin layer of aluminum is deposited atom-by-atom and is oxidized following the same process as before. This is repeated until the oxide reaches the desired thickness.

After the oxidation, an aluminum contact is deposited on top in a similar manner, introducing aluminum atoms one at a time until the aluminum contact layer is of a similar thickness to the initial aluminum substrate. In this case, the distribution of velocities is chosen to mimic the metal evaporation; see Cyster *et al.* [25] for details. The structure is then optimized using the LAMMPS energy minimization to find the lowest energy configuration of the atoms that constitute the junction. We calculate the charges of the atoms in the system, and then the Ewald summation method can ultimately be used to determine the electric potential of the system with respect to atom position [53].

This method is used with an Al (100) and Al (111) substrate for two complete simulations of each, with varying thicknesses of oxide giving 48 structures in total as shown in Table I.

## B. Characterizing the junction formation

### 1. Thickness

When simulating oxide growth, we require a measure of thickness to indicate when to stop the simulation. For this, we use the  $z$  distance from the first to last oxygen atom in the junction (oxygen extent) as an approximate guide to the barrier thickness. Table I shows these barrier thicknesses for each structure. We have also determined the full-width at half-maximum (FWHM) thickness of the barrier for each structure. This is calculated using the maximum of the average mass density across the junction shown in Fig. 6.

Due to the lower stoichiometric ratio of Al:O near the Al/AIO<sub>x</sub> interface, we expect the oxygen extents in Table I to be an overestimation of the thickness that would be measured experimentally. We include the FWHM thickness computed from the mass density as an alternate measure, however this in turn may be an underestimation. Given the ambiguity of defining oxide thickness at the atomic scale, Table I gives both values as an upper and lower limit of the thickness for a given structure. The intervals between FWHM values are multiples of 0.25 due to the bin size chosen for the rolling average of the mass density.

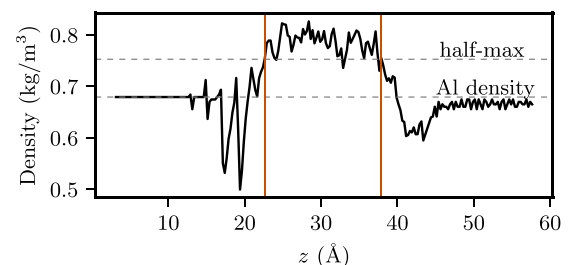


FIG. 6. The rolling average of the mass density across the thickest barrier in the “(100)1” data set. The half-max reference line is halfway between the maximum value in the data set and the Al density, where the latter is set using the mass density value at the beginning of the source contact. The solid orange lines then indicate the FWHM, which we take as the barrier thickness.

TABLE I. Summary of parameters used to characterize junction formation in this work for each data set. The number of oxygen atoms in a simulation cell is given by “no. O,” and the percentage coverage calculated using the Voronoi cells is “% coverage.” The thicknesses from the FWHM of the mass density (shown in Fig. 6) and the oxygen extent are labeled “FWHM” and “O extent,” respectively.

(100)1			(100)2			(111)1			(111)2		
no. O	% coverage										
28	27.81		20	24.28		26	25.38		24	27.38	
36	36.88		26	30.34		33	32.74		29	32.37	
56	52.77		43	46.07		46	42.75		32	35.76	
69	59.24		54	52.92		56	51.70		44	46.38	
83	68.48		68	67.06		84	63.90		58	59.08	
139	92.12		148	91.31		140	91.68		120	86.69	
no. O	FWHM	O extent									
143	4.75	10.07	150	3.00	10.25	146	4.75	10.57	134	4.25	10.46
239	6.00	12.74	158	3.25	12.44	156	4.00	12.72	206	7.25	13.40
240	6.00	14.21	243	6.75	15.50	232	7.00	14.03	245	8.00	14.77
311	8.75	16.48	250	6.00	16.81	248	9.50	16.62	269	7.75	16.64
346	9.50	20.37	255	6.00	22.89	279	10.00	19.03	306	9.00	20.66
451	15.25	23.49	383	13.50	23.49	397	15.50	24.10	399	14.50	24.09

## 2. Percentage coverage

To determine the percentage of substrate that is covered in oxygen for each of our structures, we first determine the volume occupied by oxygen atoms in the barrier region. This is done by calculating the Voronoi cell around each atom in the barrier [54–56]. Figure 7 shows oxygen volumes for a low percentage coverage ( $< 50\%$ ) barrier on the “(100)1” crystal substrate.

For clarity, Fig. 7(a) shows the Voronoi cells for just the oxygen atoms in this structure, looking down on the substrate. By projecting the 3D Voronoi cells onto a 2D plane, we can determine a ratio of uncovered to covered regions, giving the percentage of the underlying substrate that is covered. Figure 7(b) shows a percentage coverage calculation indicating areas that are covered by an oxygen Voronoi cell, and Table I shows the percentage coverage values for each structure.

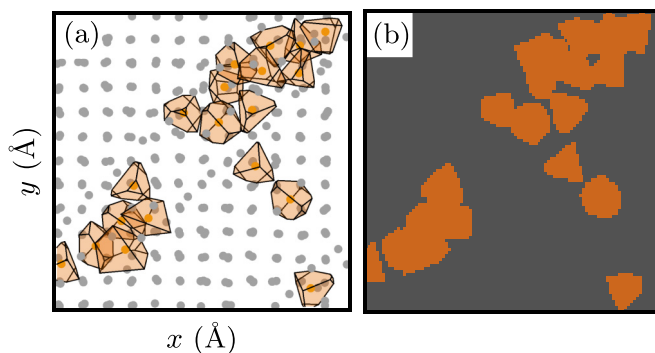


FIG. 7. (a) A three-dimensional Voronoi diagram showing the oxygen volume in a Josephson junction simulated using molecular dynamics, showing the  $xy$  plane which is perpendicular to the transport direction. Oxygen and aluminum atoms are indicated using orange and gray points, respectively. The  $z$  (transport) direction is into the page. (b) Results of surface coverage calculation for the same structure.

Comparing the various structures in Table I, we see that percentage coverage and oxygen extent increase monotonically with the number of oxygen atoms. However, the barrier FWHM (which is key for defining the transport characteristics) can vary greatly from run to run, and as a function of substrate crystal orientation. See, for example, structure “(100)2” in the range 200–300 oxygen atoms. This is because the barrier characteristics depend strongly on the microstructure details of the oxide region. Note that we do not set the thickness or the percentage coverage of a simulated junction, rather these are emergent properties of the simulation.

Figure 8 shows the relationship between the substrate coverage against the number of oxygen atoms in the barrier for the “(100)1” structure. Slices are taken at every tenth oxygen atom that is bound to the surface during oxidation in the molecular-dynamics simulation.

In Fig. 8 we see two different regimes. Below  $\sim 100$  oxygen atoms (per  $24 \text{ \AA} \times 24 \text{ \AA}$  area) we see one gradient which we attribute to individual oxygen atoms being deposited onto the metal substrate, and above  $\sim 100$  oxygen atoms we see a different gradient attributed to the formation of an oxide layer. The insets show the Voronoi surface coverages for two structures within each regime as calculated in Fig. 7. These results indicate that below  $\sim 100$  oxygen atoms is where pinhole formation is likely to occur before we see behavior consistent with a film of  $\text{AlO}_x$  as the number of oxygen atoms increases.

## IV. NORMAL TRANSPORT IN AN ATOMISTIC MODEL

Having developed an atomistic model of Al- $\text{AlO}_x$ -Al tunnel junctions using molecular dynamics, we now use this model to obtain information about the transport properties of these 3D simulated junctions. The transport calculations in this section do not include superconducting parameters or considerations of Cooper pairs of electrons. They describe the device in its normal state and are purely single-electron transport calculations.

We use a NEGF method to calculate the transmission and the normal resistance,  $R_N$ , in the same way as we did for the toy model in Sec. II B. Figure 9 shows the resultant  $R_{NA}$

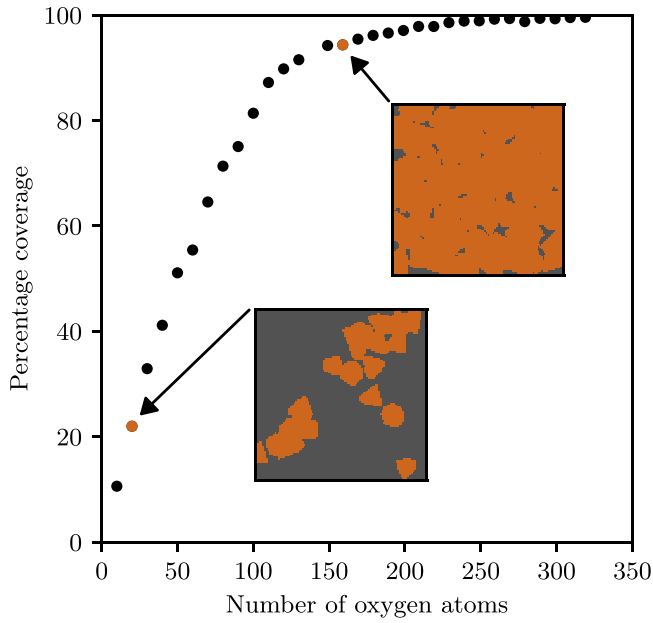


FIG. 8. The oxidation process in a molecular-dynamics simulation of  $\text{AlO}_x$  growth on the “(100)1” aluminum substrate before overgrowth with a metal contact. Data points are shown for every tenth oxygen atom that is bound to the surface. Results show the percentage of the aluminum substrate that is covered by oxygen atoms as a function of the number of oxygen atoms in the insulating barrier with a cross-sectional area of  $576 \text{ \AA}^2$ .

relationship for junctions grown on each substrate. As we expect  $R_{NA}$  to be exponential with film thickness [57], results are plotted on a logarithmic scale.

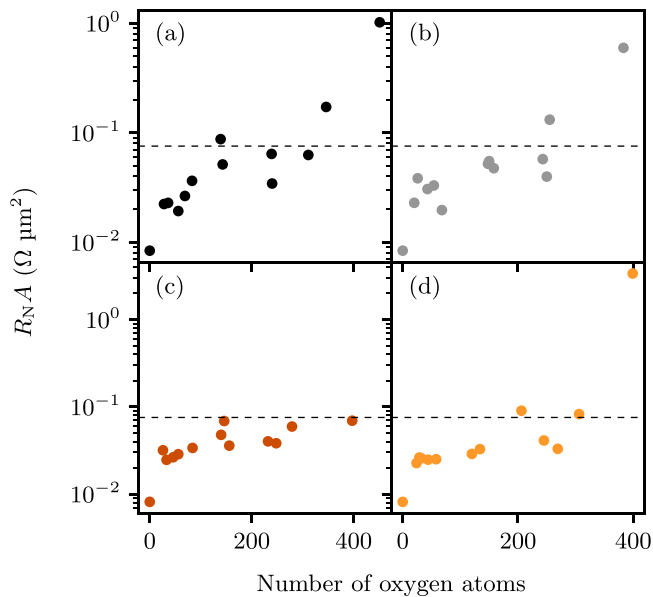


FIG. 9. Resistance area for Al- $\text{AlO}_x$ -Al junctions with increasing numbers of oxygen atoms in the barrier. Each panel shows data for structures grown on different aluminum substrates, and two calculations of each. The structures for each panel are (a) “(100)1,” (b) “(100)2,” (c) “(111)1,” and (d) “(111)2.”

On each of the data sets in Fig. 9 the dashed line indicates the resistance quantum that corresponds to  $T = 1$  as determined in Fig. 3. It corresponds to the expected transition from metallic to insulating behavior. For every data set we see significant variation in the resistance values, and no clear transition to insulating behavior until 400 oxygen atoms are deposited. An exception to this is in the “(111)1” data set, where we find that the last data point is below the metal-to-insulator transition even with approximately 400 oxygen atoms in the barrier, like the other structures. This implies there may be more metallic regions present in the barrier in the form of pinholes or weak-points.

In this study, we aim to create a distinction between pinholes and weak-points. We define pinholes to be present when the Al substrate is  $< 100\%$  covered in oxide, which results in a direct metallic link once metal is deposited as a top contact (as in Sec. II B). We define weak-points to be present when our surface coverage calculations show no presence of pinholes, however the transport calculations indicate a localized higher current density compared to a uniform barrier. Such localized variation in the current density results from variation in the oxide density or stoichiometry but may not correspond to the conventional image of a pinhole, as illustrated in Fig. 1.

Comparing these results to Fig. 8, we find that an increase in surface coverage (especially close to 100%) is not directly correlated to insulating behavior in the barrier. We reach close to 100% coverage when approximately 200 oxygen atoms are deposited, however for all data sets in Fig. 9 we see that the  $R_{NA}$  data points around 200 oxygen atoms are close to or below the metal-to-insulator transition, indicating metallic behavior. This highlights that surface coverage alone cannot give us a good indication of a functioning barrier.

The variation we see in the resistance data in Fig. 9 is consistent with measurements in manufactured Al- $\text{AlO}_x$ -Al tunnel junctions [9–11]. For example, it has been shown that when some device barriers are grown to thicknesses that are typically expected to display insulating behavior, a few may fail due to an excess current [20]. Data set “(111)1” shows a theoretical example that could explain these situations. As well as this, experiments have shown significant variability in the transport between devices fabricated in the same way. We believe these variabilities may arise from the disordered nature of the  $\text{AlO}_x$  region as results in Fig. 3 showed significantly less variability, likely due to the uniform potential barrier used and systematic changes to the pinhole size. It has also previously been shown that crystal grain boundaries in the aluminum bottom contact could cause thickness variations in the  $\text{AlO}_x$  layer that is grown above [52]. These thickness variations could then in turn cause irregularities in the transport measurements. In this study, we have not included the effects of grain boundaries, and we grow devices on single-crystal aluminum substrates. Despite omitting grain boundaries, we still see significant variability, highlighting that disorder alone may be a key contributor to the variation in transport we see in junctions of this sort.

There also appears to be a larger spread in the data for junctions grown on Al(100) substrates compared to Al(111). This could indicate that the spatial variation of the junction resistance for the (111) crystal orientation is lower, however further statistics are required to be definitive. The

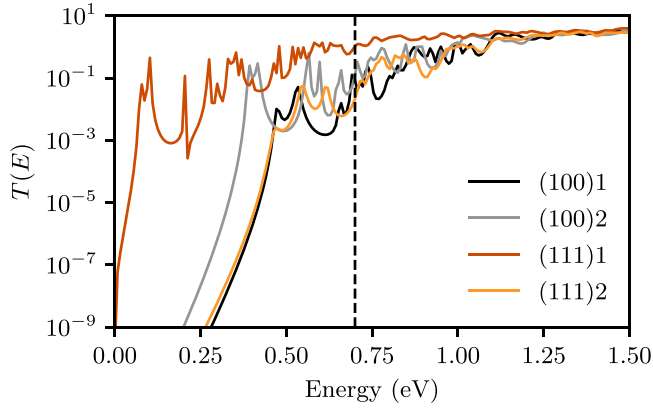


FIG. 10. Transmission functions for the thickest barriers in each of our data sets. The dashed line indicates  $E_F = 0.7$  eV, which is used for the calculations in this work.

computational expense of growing large atomic structures and performing atomic-resolution transport calculations limits our ability to perform detailed replication studies at this time.

In prior work by Cyster *et al.* [27], a reliable exponential trend was observed in  $R_N A$  calculations for junctions with increasing thickness. That work used a melt and quench method to create devices that gave control over the oxide thickness, however it did not consider the experimental fabrication processes used. In this study, we mimic the fabrication process more closely [25], aiming to provide a more accurate representation of what would be obtained from measurements of real devices. However, this does produce greater variability in the transport results. Cyster *et al.* [27] also use an SM potential, whereas this work uses a ReaxFF potential, which has since been shown to more accurately describe the self-limiting behavior we see experimentally [25].

To investigate the variation we see in the transport calculations, Fig. 10 shows the transmission function for each of the thickest structures, corresponding to more than 350 oxygen atoms in the simulation cell.

In particular, Fig. 10 shows the sensitivity of transport measurements to changes in the Fermi energy, noting that our calculations all use  $E_F = 0.7$  eV, marked in Fig. 10 with a dashed line. From the transmission we also see that the “(111)1” structure is more transparent than the other three structures, supporting results from Fig. 9 where we found that the thickest structure was metallic compared to the junctions in the other data sets.

Our calculations discussed up to this point give us an indication of the overall transport in the junction. However, to understand the specific effects that pinholes have on transport within the barrier, we need to study how current flows through the junction spatially. To investigate this, we calculate the three-dimensional current density throughout the junction.

The current flowing between two points in a junction is given by the elementwise product of  $H$  and  $G^n$ ,

$$J(\mathbf{r}, \mathbf{r}', E) = \frac{e}{h} \text{Im}[H \circ G^n], \quad (11)$$

where the electron Green’s function is given by

$$G^n(E) = G^r \Sigma^{\text{in}} G^a \quad (12)$$

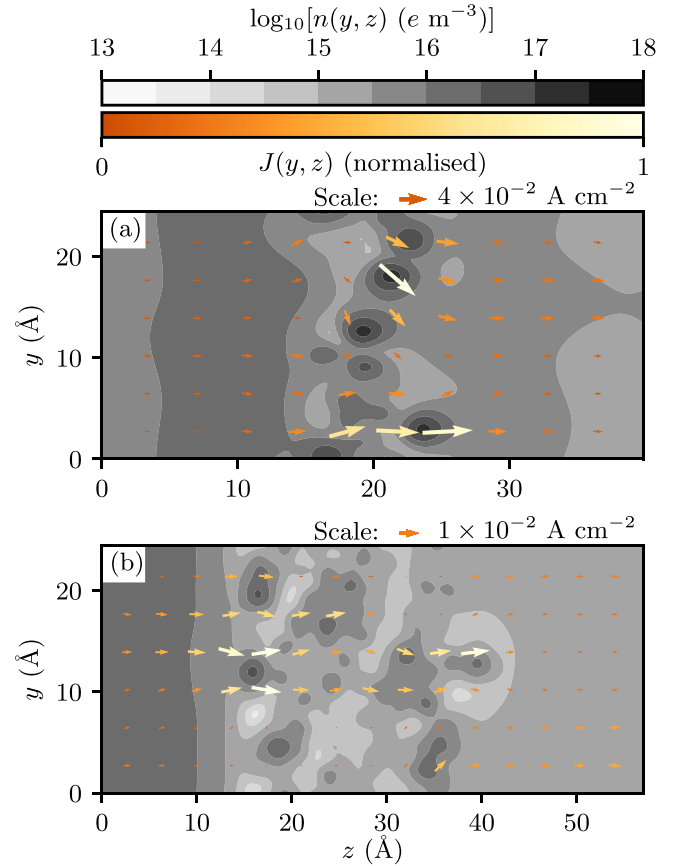


FIG. 11. Orange arrows show the current density through the “(111)1” device for (a) the lowest coverage structure with no. O = 26 (pinholes), and (b) the thickest barrier (comparable to a fabricated device) with no. O = 397. Charge density throughout the junction is shown in grayscale. Orange arrows show the localized current densities. The arrow scale indicates the magnitude of the current density, and the arrow color table is normalized.

and

$$\Sigma^{\text{in}}(E) = \Gamma_S f_S + \Gamma_D f_D. \quad (13)$$

Using  $G^n(E)$ , the charge density can be calculated in three dimensions with

$$n(x, y, z) = \frac{1}{2\pi a_x a_y a_z} \text{diag}(G^n(E)). \quad (14)$$

The current in one direction is calculated from the difference between pairs of points. For the  $z$  direction this looks like

$$J_z(x, y, z; E) = \frac{1}{a_x a_y} [J(\mathbf{r}, \mathbf{r}', E) - J(\mathbf{r}', \mathbf{r}, E)]. \quad (15)$$

Figure 11 shows  $yz$  slices of the barrier and the charge and current densities for positions in those slices.

Dark regions in Fig. 11 correspond to areas in the junction that have a higher charge density, typically indicative of a metallic region. The orange arrows show the single-electron current density at positions in the junction. In both figures it is apparent that the largest proportion of current flows through localized regions of the junction. Figure 11(a) shows the lowest surface coverage junction in the “(111)1” data set

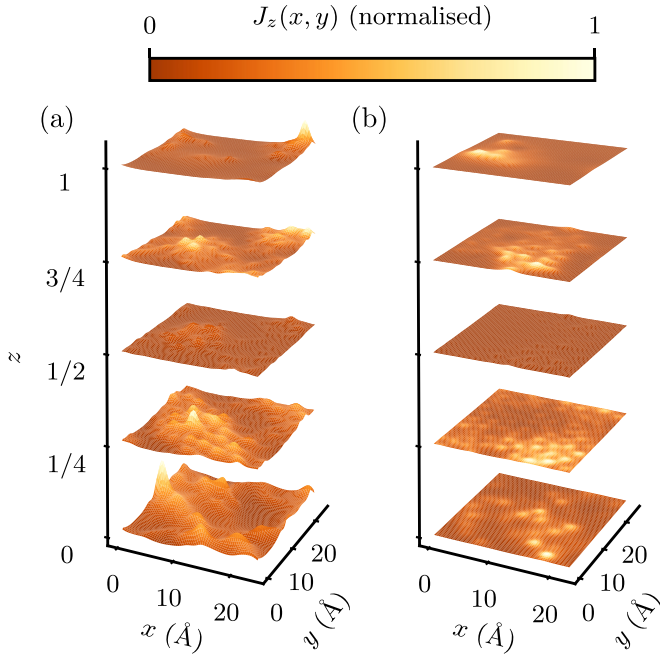


FIG. 12. Current density  $xy$  slices through the transport direction,  $z$ , for the thickest barriers in the (a) “(100)1” and (b) “(111)2” device. Slices are taken at regular  $z$  intervals through the barrier region as fractions of the oxygen extent in each junction. Current densities are normalized by the maximum in the “(100)1” data set.

(26 oxygen atoms), and Fig. 11(b) shows the same substrate but for the thickest oxide for full surface coverage (397 oxygen atoms). The current in Fig. 11(a) is on average approximately four times higher than in Fig. 11(b) as is expected for a more transparent barrier. Of particular interest is that, despite the device in Fig. 11(b) having a thick enough barrier to expect insulating behavior, there are still weak-points that facilitate peaks in the single-electron current flow.

The “(111)1” structure shown in Fig. 11(b) is the same device that has displayed a higher transparency in Figs. 10 and 9(c). Figure 11 allows us to probe how the microscopic structure of the device may contribute to the higher transparency across the junction, emphasizing that the disordered barrier may be a crucial consideration when trying to predict the parameters of fabricated Josephson junction devices.

In general, defects in a superconducting qubit can couple via charge, flux, or critical current in the circuit [58]. In the case when defects in the junction modulate the critical current [16,17], the qubit-defect coupling strength is proportional to the magnitude of the (normal or super) current flow at the site of the defect. Therefore, increased variance in the current density through the junction can result in increased coupling to defects.

Figure 12 shows  $xy$  slices of the magnitude of the current density perpendicular to the transport direction for the thickest barriers in “(100)1” and “(111)2” data sets. For figures that follow, we compare the “(100)1” and “(111)2” data sets where the thickest two barriers are both insulating.

The slices shown in Fig. 12 are taken at equal intervals through the oxygen extent of the barrier region. The distribution of the current density between slices varies greatly;

specifically, we see that the current peaks in different positions between slices. This highlights that for thicker structures without clear pinholes in the oxide, we find weaker, indirect paths of single-electron current (weak-points). We suspect this is due to aluminum-rich regions in the oxide enabling a current flow with an indirect path. It is important to note that the edges of the oxide are not abrupt as there is significant oxygen diffusion into the contacts [22,25]. This stoichiometric gradient results in more current hot spots at the starts and ends of the oxide compared to the middle of a junction. The central slices from Fig. 12 are then the most indicative of the behavior of the insulating barrier in the junction.

Although these weak-points have the most significant effect in the “(111)1” data set, they are nonetheless present in all junctions studied in this work.

## V. SUPERCONDUCTING TRANSPORT IN AN ATOMISTIC MODEL

Higher transparency channels within the tunnel barrier in Josephson junctions can cause variations in the transmission-dependent CPR [21]. The results in Sec. IV indicate higher transparency regions in the normal current density. Following the same methods used in Sec. II C for the toy model, we determine the transmission eigenvalues and CPR for each structure.

In this section, we also follow recent work which shows that the contributions from different transmission channels can be written as a Fourier series [21]:

$$I_S(\phi) = \sum_{m=1}^{\infty} c_m \sin(m\phi), \quad (16)$$

where  $c_m$  are the transmission-dependent Fourier coefficients of order  $m$ .

The ratio of the fundamental sinusoidal signal to the higher-order contributions is given by

$$\nu = \frac{1}{c_1} \sum_{m=2}^{\infty} c_m, \quad (17)$$

which allows us to quantify how sinusoidal the CPR is.

Figure 13 shows the CPR and Fourier components calculated for three structures within the “(100)1” data set.

The magnitudes of the CPRs in Fig. 13(a) differ by orders of magnitude. For this reason, we choose to scale them by the critical current,  $I_C$ , which is equivalent to the maximum for each curve. These values are given in the caption and vary between structure. We find the structures with the least amount of oxygen to have a higher  $I_C$  compared to the thickest barriers. Scaling the results in Fig. 13(a) allows us to more clearly study the shape of the CPR. For lower surface coverages, we see a deviation from the expected sinusoidal Josephson relationship,  $I_S(\phi) = \sin \phi$  [21,41]. When we look at the Fourier transform of each  $I_S$  curve, we find that for junctions with 27.81% and 59.24% coverage there are extra contributions in the Fourier series expansion in Eq. (16). These arise from the higher transmission probability eigenvalues for the thinner barrier structures, and result in a deviation from the sinusoidal relationship. To show this clearly, Figs. 13(b), 13(c) and 13(d) give a breakdown of different sinusoidal contributions to the

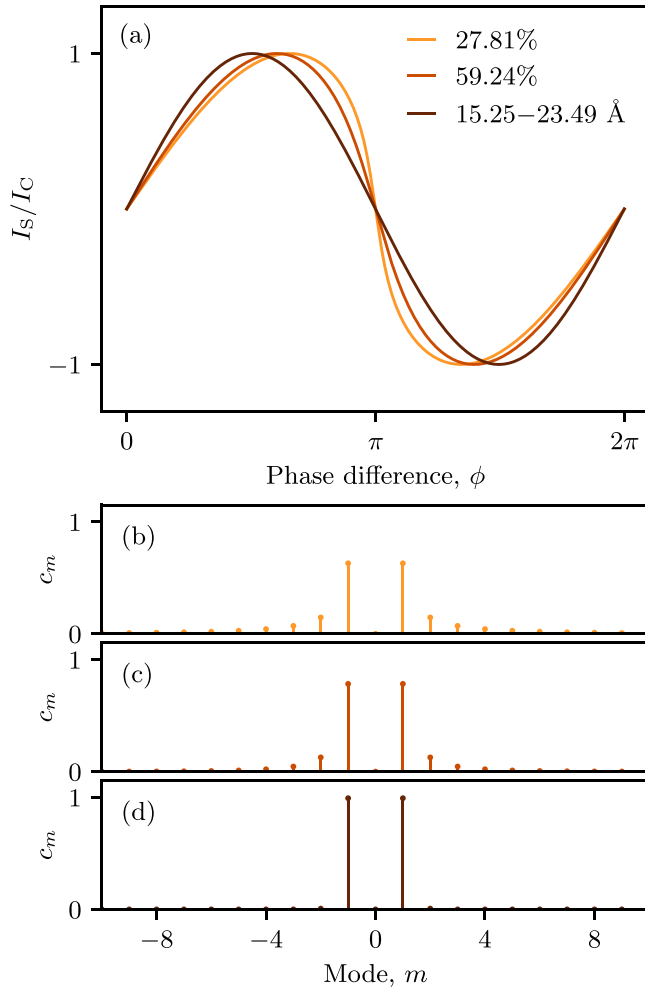


FIG. 13. (a) CPRs for structures within the “(100)1” data set, as labeled in the legend. Each curve is normalized by the critical current,  $I_C = 0.169, 0.132,$  and  $0.003 \mu\text{A}$  for the 27.81%, 59.24%, and 15.25–23.49 Å structures, respectively, all of which have a cross-sectional area of  $24 \times 24 \text{ \AA}^2$ . (b)–(d) The frequency domain representation of each of the curves in (a), highlighting the different sinusoidal contributions to each signal. The Fourier coefficients,  $c_m$ , are normalized such that their sum equals 1.

CPR. Most notably, the thickest junction shown in Fig. 13(d) has only one significant contribution, the main sinusoidal signal, and is the closest to an ideal Josephson junction. As discussed in Sec. II C, although we see a systematic change toward sinusoidal behavior in Fig. 13, this is not necessarily indicative of every structure in the data set. The shape of the CPR is dependent on the number of channels with transmission probabilities close to 1, which in turn depends on the structure of the oxide and the presence of pinholes. Figure 14 summarizes data from Fig. 13 for all the structures in the “(100)1” and “(111)2” data sets, including the transmission eigenvalues for the “(100)1” structure.

Figure 14(a) shows the “(100)1” set of data for the eigenvalues of the transmission matrix calculated from the Green’s function. We see that for thinner barriers, the eigenvalues are closer to 1, indicating a more transparent junction. As the barriers become thicker, the eigenvalues begin to drop to zero.

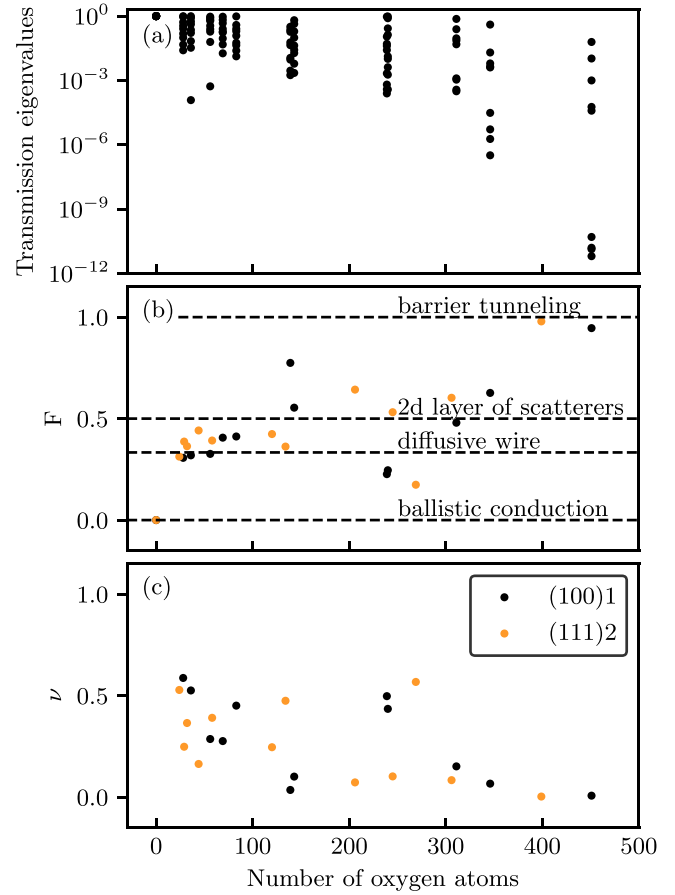


FIG. 14. (a) Eigenvalues of the transmission matrix for the “(100)1” data set. (b) Fano factors for each structure in the “(100)1” data set (black) and “(111)2” data set (orange); dashed lines indicate different types of nanoscale conduction from the literature. (c) The ratio of higher-order Fourier coefficients to the fundamental coefficient. A value of zero corresponds to a purely sinusoidal signal.

The Fano factor, shown in Fig. 14(b), is given by

$$F = \frac{\sum_n T_n(1 - T_n)}{\sum_n T_n}, \quad (18)$$

which allows us to differentiate between different types of nanoscale conduction [59]. We find that as we grow thicker barriers the Fano factor approaches 1, indicating barrier tunneling, and for pure aluminum we obtain a Fano factor of 0 corresponding to ballistic transport as indicated on the graph with dashed lines. A Fano factor of  $1/3$  corresponds to a diffusive wire, and  $1/2$  a 2D layer of randomly distributed scatterers [29,59]. We note that many of the points in the thinner barriers are situated around the diffusive wire regime, and we also see a few points near the 2D layer of the scatterers regime. However, given the variability in our data, we cannot distinguish between these two regimes definitively.

Due to the logarithmic scale in Fig. 14(a) for the “(100)1” data set, the results in Figs. 14(b) and 14(c) for the same data set may show a greater discrepancy (by eye) compared to the eigenvalues in Fig. 14(a). Figure 14(c) shows the ratio of the largest sinusoidal contribution to the CPR with the other contributions, highlighting results in Fig. 13 which indicate that

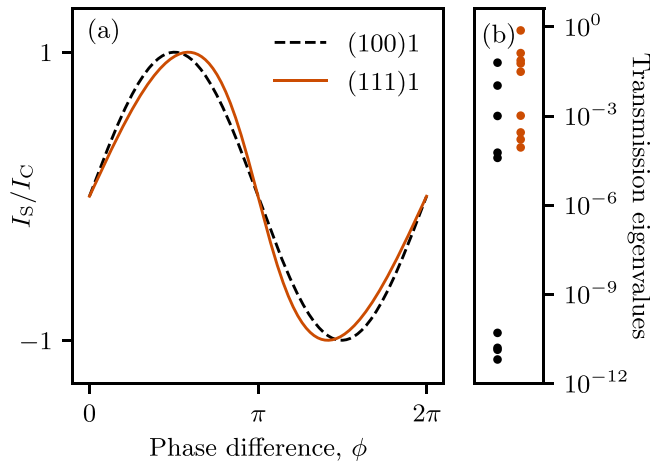


FIG. 15. (a) CPRs for the thickest structures in the “(100)1” and “(111)1” data sets. Each curve is normalized by the critical current. (b) The transmission matrix eigenvalues for the same two structures. For the “(100)1” and “(111)1” structure, respectively,  $\nu = 0.0071$  and  $0.1777$ .

thicker barriers approach a pure sinusoidal CPR and a  $\nu \simeq 0$ , indicative of an ideal Josephson junction. For the “(100)1” data set, the junction with the strongest sinusoidal response in Fig. 14, with  $\nu = 0.0071$ , has a thickness between 15.25 and 23.49 Å based on the FWHM and O extent in Table I. Figure 14 indicates that lower oxygen content in the barrier region leads to channels with higher transmission probabilities, resulting in a deviation from the expected sinusoidal response. This is particularly true for thinner barriers where pinholes are more likely to be present. In Sec. IV we found an anomaly in the thickest barrier for the “(111)1” data set, where there were no pinholes present, however there were weak-points in the barrier. The term weak-points is synonymous with channels that have higher transmission probabilities.

Figure 15 directly compares the “(111)1” data set to the “(100)1” for the thickest barriers. Figure 15(b) shows the larger proportion of higher transmission eigenvalues for the “(111)1” data set compared to the “(100)1” data set. As we found for junctions with pinholes, these higher transmission channels result in extra contributions to the CPR given in Eq. (16). Figure 15(a) shows how this results in a deviation from the expected sinusoidal response, which “(100)1” shows an example of based on its  $\nu$  ratio given in Fig. 14(c) and in the caption of Fig. 15. How pure the sinusoidal response is has a direct influence on the effective Hamiltonian in superconducting qubits. To accurately calibrate qubits, it is essential to be able to predict the CPR [21]. Our results indicate that both pinholes and weak-points in the barrier can lead to corrections to the conventional sinusoidal response.

## VI. CONCLUSION

The results of this work show the key role that both pinholes and disorder in the amorphous oxide barrier play in Al-AIO<sub>x</sub>-Al tunnel junctions. Prior work has shown variations in the critical current of Josephson junction devices

fabricated in the same way. Using molecular dynamics, we have been able to probe the microscopic structure of these devices and analyze the oxidation process step-by-step. We have shown that in thinner barriers pinholes may be present and be a source of single-electron current, which could in turn affect the transport properties of Josephson junction devices. In addition, we have also observed a significant amount of variability in junctions with a complete barrier, which appears to be caused by the inherently disordered oxide barrier. To understand the minimum amount of oxide required to have a functioning device, we studied the metal-insulator transition and found that for a uniform electric potential we should see a transition to insulating behavior between 90% and 100% coverage. In reality, the amorphous structure of the oxide creates a nonuniform electric potential, which makes this transition less clear. In fact, even when barriers are grown to have thicknesses comparable to experimentally fabricated devices, we might not see a transition to insulating behavior, which could be a contributing factor to device failure. These devices do not have pinholes in the barrier, but have weak-points that can facilitate single-electron current flow.

We find that the variations in transport that arise from the nonuniform electric potential also have consequences on the CPR. More transmissible channels due to pinholes result in more contributions to the CPR, causing it to deviate from the expected pure sinusoidal signal. As barriers are grown thicker, we obtain a stronger sinusoidal signal. Although this is the case, we also find that weak-points in the barrier (in addition to fully metallic pinholes) can lead to corrections to the conventional sinusoidal response. This emphasizes that it is not only essential that a Josephson junction be free of pinholes but also that the oxide barrier be as uniform as possible. Such precise control of junction thickness, density, and stoichiometry may ultimately only be possible with epitaxial junctions [16,60,61].

Previously, the specific processes of oxide growth and why thinner films may not function as expected were not well understood. Our work uses computational models to analyze the oxidation process and the formation of structures that may cause faults in junctions with oxide barriers. The analysis in this work aims to inform and support Al-AIO<sub>x</sub>-Al device fabrication.

## ACKNOWLEDGMENTS

The authors acknowledge the support of the Australian Research Council through grants CE170100039, and the National Computation Infrastructure (NCI), which provided the computational resources to undertake this work. The authors also acknowledge useful discussions with B. Muralidharan and I. Pop, and the assistance of L. Moshovelis with the creation of Fig. 1. We acknowledge the people of the Woiwurrung, Wathawurrung, and Boonwurrung language groups as the traditional custodians of the land on which this research was conducted, and the people of the Ngannawal language group who are the Traditional Custodians of the land of the Australian Capital Territory where NCI is located.

- [1] M. A. Nielsen and I. L. Chuang, *Quantum Computation and Quantum Information* (Cambridge University Press, Cambridge, 2010).
- [2] A. M. Zagoskin, *Quantum Engineering: Theory and Design of Quantum Coherent Structures* (Cambridge University Press, Cambridge, 2011).
- [3] G. Wendin and V. S. Shumeiko, Quantum bits with Josephson junctions (Review Article), *Low Temp. Phys.* **33**, 724 (2007).
- [4] Z. Chen, K. J. Satzinger, J. Atalaya, A. N. Korotkov, A. Dunsworth, D. Sank, C. Quintana, M. McEwen, R. Barends, P. V. Klimov, S. Hong, C. Jones, A. Petukhov, D. Kafri, S. Demura, B. Burkett, C. Gidney, A. G. Fowler, A. Paler, H. Putterman *et al.*, Exponential suppression of bit or phase errors with cyclic error correction. *Nature (London)* **595**, 383 (2021).
- [5] Y. Kim, A. Eddins, S. Anand, K. X. Wei, E. van den Berg, S. Rosenblatt, H. Nayfeh, Y. Wu, M. Zaletel, K. Temme, and A. Kandala, Evidence for the utility of quantum computing before fault tolerance, *Nature (London)* **618**, 500 (2023).
- [6] M. Kjaergaard, M. E. Schwartz, J. Braumüller, P. Krantz, J. I. Wang, S. Gustavsson, and W. D. Oliver, Superconducting qubits: Current state of play, *Annu. Rev. Condens. Matter Phys.* **11**, 369 (2020).
- [7] M. Carroll, S. Rosenblatt, P. Jurcevic, I. Lauer, and A. Kandala, Dynamics of superconducting qubit relaxation times, *npj Quantum Inf.* **8**, 132 (2022).
- [8] C. Müller, J. Lisenfeld, A. Shnirman, and S. Poletto, Interacting two-level defects as sources of fluctuating high-frequency noise in superconducting circuits, *Phys. Rev. B* **92**, 035442 (2015).
- [9] J. M. Kreikebaum, K. P. O'Brien, A. Morvan, and I. Siddiqi, Improving wafer-scale Josephson junction resistance variation in superconducting quantum coherent circuits, *Supercond. Sci. Technol.* **33**, 06LT02 (2020).
- [10] A. Osman, J. Simon, A. Bengtsson, S. Kosen, P. Krantz, D. P. Lozano, M. Scigliuzzo, P. Delsing, J. Bylander, and A. Fadavi Roudsari, Simplified Josephson-junction fabrication process for reproducibly high-performance superconducting qubits, *Appl. Phys. Lett.* **118**, 064002 (2021).
- [11] J. Verjauw, R. Acharya, J. Van Damme, T. Ivanov, D. P. Lozano, F. A. Mohiyaddin, D. Wan, J. Jussot, A. M. Vadiraj, M. Mongillo, M. Heyns, I. Radu, B. Govoreanu, and A. Potočnik, Path toward manufacturable superconducting qubits with relaxation times exceeding 0.1 ms, *npj Quantum Inf.* **8**, 93 (2022).
- [12] D. J. Van Harlingen, T. L. Robertson, B. L. T. Plourde, P. A. Reichardt, T. A. Crane, and J. Clarke, Decoherence in Josephson-junction qubits due to critical-current fluctuations, *Phys. Rev. B* **70**, 064517 (2004).
- [13] M. Werninghaus, D. J. Egger, and S. Filipp, High-speed calibration and characterization of superconducting quantum processors without qubit reset, *PRX Quantum* **2**, 020324 (2021).
- [14] N. Wittler, F. Roy, K. Pack, M. Werninghaus, A. S. Roy, D. J. Egger, S. Filipp, F. K. Wilhelm, and S. Machnes, Integrated tool set for control, calibration, and characterization of quantum devices applied to superconducting qubits, *Phys. Rev. Appl.* **15**, 034080 (2021).
- [15] T. M. Hazard, W. Woods, D. Rosenberg, R. Das, C. F. Hirjibehedin, D. K. Kim, J. M. Knecht, J. Mallek, A. Melville, B. M. Niedzielski, K. Serniak, K. M. Sliwa, D. R. W. Yost, J. L. Yoder, W. D. Oliver, and M. E. Schwartz, Characterization of superconducting through-silicon vias as capacitive elements in quantum circuits, *Appl. Phys. Lett.* **123**, 154004 (2023).
- [16] C. Müller, J. H. Cole, and J. Lisenfeld, Towards understanding two-level-systems in amorphous solids: Insights from quantum circuits, *Rep. Prog. Phys.* **82**, 124501 (2019).
- [17] M. Constantin and C. C. Yu, Microscopic model of critical current noise in Josephson junctions, *Phys. Rev. Lett.* **99**, 207001 (2007).
- [18] X. Zhou, H. Wadley, and D. Wang, Transient hole formation during the growth of thin metal oxide layers, *Comput. Mater. Sci.* **39**, 794 (2007).
- [19] T. Greibe, M. P. V. Stenberg, C. M. Wilson, T. Bauch, V. S. Shumeiko, and P. Delsing, Are “pinholes” the cause of excess current in superconducting tunnel junctions? A study of andreev current in highly resistive junctions, *Phys. Rev. Lett.* **106**, 097001 (2011).
- [20] S. K. Tolpygo and D. Amparo, Electrical stress effect on Josephson tunneling through ultrathin AlO<sub>x</sub> barrier in Nb/Al/AlO<sub>x</sub>/Nb junctions, *J. Appl. Phys.* **104**, 063904 (2008).
- [21] D. Willsch, D. Rieger, P. Winkel, M. Willsch, C. Dickel, J. Krause, Y. Ando, R. Lescanne, Z. Leghtas, N. T. Bronn, P. Deb, O. Lanes, Z. K. Mineev, B. Dennig, S. Geisert, S. Günzler, S. Ihssen, P. Paluch, T. Reisinger, R. Hanna *et al.*, Observation of Josephson harmonics in tunnel junctions, *Nat. Phys.* (2024).
- [22] L. Zeng, D. T. Tran, C.-W. Tai, G. Svensson, and E. Olsson, Atomic structure and oxygen deficiency of the ultrathin aluminium oxide barrier in Al/AlO<sub>x</sub>/Al Josephson junctions, *Sci. Rep.* **6**, 29679 (2016).
- [23] H. Schulze, R. Behr, F. Müller, and J. Niemeyer, Nb/Al/AlO<sub>x</sub>/AlO<sub>x</sub>/Al/Nb Josephson junctions for programmable voltage standards, *Appl. Phys. Lett.* **73**, 996 (1998).
- [24] S. Morohashi, F. Shinoki, A. Shoji, M. Aoyagi, and H. Hayakawa, High quality Nb/Al-AlO<sub>x</sub>/Nb Josephson junction, *Appl. Phys. Lett.* **46**, 1179 (1985).
- [25] M. J. Cyster, J. S. Smith, N. Vogt, G. Opletal, S. P. Russo, and J. H. Cole, Simulating the fabrication of aluminium oxide tunnel junctions, *npj Quantum Inf.* **7**, 12 (2021).
- [26] S. Datta, *Quantum Transport: Atom to Transistor* (Cambridge University Press, Cambridge, 2005).
- [27] M. J. Cyster, J. S. Smith, J. A. Vaitkus, N. Vogt, S. P. Russo, and J. H. Cole, Effect of atomic structure on the electrical response of aluminum oxide tunnel junctions, *Phys. Rev. Res.* **2**, 013110 (2020).
- [28] M. Tinkham, *Introduction to Superconductivity*, 2nd ed. (Dover, Mineola, NY, 2004).
- [29] T. T. Heikkilä, *The Physics of Nanoelectronics: Transport and Fluctuation Phenomena at Low Temperatures*, 21st ed. (Oxford University Press, Oxford, 2013).
- [30] X. W. Zhou and H. N. G. Wadley, Atomistic simulation of AlO<sub>x</sub> magnetic tunnel junction growth, *Phys. Rev. B* **71**, 054418 (2005).
- [31] A. Presland, G. Price, and D. Trimm, Kinetics of hillock and island formation during annealing of thin silver films, *Prog. Surf. Sci.* **3**, 63 (1972).
- [32] A. Bilmes, S. Volosheniuk, A. V. Ustinov, and J. Lisenfeld, Probing defect densities at the edges and inside Josephson junctions of superconducting qubits, *npj Quantum Inf.* **8**, 24 (2022).
- [33] H. J. Mamin, E. Huang, S. Carnevale, C. T. Rettner, N. Arellano, M. H. Sherwood, C. Kurter, B. Trimm, M. Sandberg,

- R. M. Shelby, M. A. Mueed, B. A. Madon, A. Pushp, M. Steffen, and D. Rugar, Merged-element transmons: Design and qubit performance, *Phys. Rev. Appl.* **16**, 024023 (2021).
- [34] S. Datta, *Electronic Transport in Mesoscopic Systems* (Cambridge University Press, Cambridge, 1997).
- [35] T. Ozaki, K. Nishio, and H. Kino, Efficient implementation of the nonequilibrium Green function method for electronic transport calculations, *Phys. Rev. B* **81**, 035116 (2010).
- [36] P. Sriram, S. S. Kalantre, K. Gharavi, J. Baugh, and B. Muralidharan, Supercurrent interference in semiconductor nanowire Josephson junctions, *Phys. Rev. B* **100**, 155431 (2019).
- [37] T. Aref, A. Averin, S. van Dijken, A. Ferring, M. Koberidze, V. F. Maisi, H. Q. Nguyend, R. M. Nieminen, J. P. Pekola, and L. D. Yao, Characterization of aluminum oxide tunnel barriers by combining transport measurements and transmission electron microscopy imaging, *J. Appl. Phys.* **116**, 073702 (2014).
- [38] W. Haberkorn, H. Knauer, and J. Richter, A theoretical study of the current-phase relation in Josephson contacts, *Phys. Status Solidi A* **47**, K161 (1978).
- [39] C. W. J. Beenakker, Universal limit of critical-current fluctuations in mesoscopic Josephson junctions, *Phys. Rev. Lett.* **67**, 3836 (1991).
- [40] C. Kittel, *Solid State Physics*, 8th ed. (John Wiley & Sons, New Jersey, 1955).
- [41] A. A. Golubov, M. Y. Kupriyanov, and E. Il'ichev, The current-phase relation in Josephson junctions, *Rev. Mod. Phys.* **76**, 411 (2004).
- [42] C. D. Nugroho, V. Orlyanchik, and D. J. Van Harlingen, Low frequency resistance and critical current fluctuations in Al-based Josephson junctions, *Appl. Phys. Lett.* **102**, 142602 (2013).
- [43] M. Paulsson and M. Brandbyge, Transmission eigenchannels from nonequilibrium Green's functions, *Phys. Rev. B* **76**, 115117 (2007).
- [44] M. Bürkle, J. K. Viljas, D. Vonlanthen, A. Mishchenko, G. Schön, M. Mayor, T. Wandlowski, and F. Pauly, Conduction mechanisms in biphenyl dithiol single-molecule junctions, *Phys. Rev. B* **85**, 075417 (2012).
- [45] K. Cedergren, S. Kafanov, J. L. Smirr, J. H. Cole, and T. Duty, Parity effect and single-electron injection for Josephson junction chains deep in the insulating state, *Phys. Rev. B* **92**, 104513 (2015).
- [46] A. Furusaki, H. Takayanagi, and M. Tsukada, Josephson effect of the superconducting quantum point contact, *Phys. Rev. B* **45**, 10563 (1992).
- [47] S. Plimpton, Fast parallel algorithms for short-range molecular dynamics, *J. Comput. Phys.* **117**, 1 (1995).
- [48] A. P. Thompson, H. M. Aktulga, R. Berger, D. S. Bolintineanu, W. M. Brown, P. S. Crozier, P. J. in 't Veld, A. Kohlmeyer, S. G. Moore, T. D. Nguyen, R. Shan, M. J. Stevens, J. Tranchida, C. Trott, and S. J. Plimpton, LAMMPS - a flexible simulation tool for particle-based materials modeling at the atomic, meso, and continuum scales, *Comput. Phys. Commun.* **271**, 108171 (2022).
- [49] A. C. T. van Duin, S. Dasgupta, F. Lorant, and W. A. Goddard, ReaxFF: A reactive force field for hydrocarbons, *J. Phys. Chem. A* **105**, 9396 (2001).
- [50] H. Aktulga, J. Fogarty, S. Pandit, and A. Grama, Parallel reactive molecular dynamics: Numerical methods and algorithmic techniques, *Parallel Comput.* **38**, 245 (2012).
- [51] G. J. Dolan, Offset masks for lift-off photoprocessing, *Appl. Phys. Lett.* **31**, 337 (1977).
- [52] S. Fritz, L. Radtke, R. Schneider, M. Weides, and D. Gerthsen, Optimization of Al/AlOx/Al-layer systems for Josephson junctions from a microstructure point of view, *J. Appl. Phys.* **125**, 165301 (2019).
- [53] P. P. Ewald, Die Berechnung optischer und elektrostatischer Gitterpotentiale, *Ann. Phys.* **369**, 253 (1921).
- [54] G. Voronoi, Nouvelles applications des paramètres continus à la théorie des formes quadratiques. Deuxième mémoire. Recherches sur les paralléloèdres primitifs, *J. Reine Angew. Math. (Crelles J.)* **1908**, 198 (1908).
- [55] A. V. Anikeenko, M. G. Alinchenko, V. P. Voloshin, N. N. Medvedev, M. L. Gavrilova, and P. Jedlovsky, Implementation of the Voronoi-Delaunay Method for Analysis of Intermolecular Voids, in *Computational Science and Its Applications—ICCSA 2004: International Conference, Assisi, Italy, 2004, Proceedings, Part III 4* (Springer, Berlin, Heidelberg, 2004), Vol. 3045, pp. 217–226.
- [56] M. Herceg, M. Kvasnica, C. N. Jones, and M. Morari, Multi-Parametric Toolbox 3.0, in *Proceedings of the European Control Conference (Zürich, Switzerland, 2013)*, pp. 502–510.
- [57] L. S. Dorneles, D. M. Schaefer, M. Carara, and L. F. Schelp, The use of Simmons' equation to quantify the insulating barrier parameters in Al/AlOx/Al tunnel junctions, *Appl. Phys. Lett.* **82**, 2832 (2003).
- [58] J. H. Cole, C. Müller, P. Bushev, G. J. Grabovskij, J. Lisenfeld, A. Lukashenko, A. V. Ustinov, and A. Shnirman, Quantitative evaluation of defect-models in superconducting phase qubits, *Appl. Phys. Lett.* **97**, 252501 (2010).
- [59] Y. Blanter and M. Büttiker, Shot noise in mesoscopic conductors, *Phys. Rep.* **336**, 1 (2000).
- [60] J. S. Kline, M. R. Vissers, F. C. S. da Silva, D. S. Wisbey, M. Weides, T. J. Weir, B. Turek, D. A. Braje, W. D. Oliver, Y. Shalibo, N. Katz, B. R. Johnson, T. A. Ohki, and D. P. Pappas, Sub-micrometer epitaxial Josephson junctions for quantum circuits, *Supercond. Sci. Technol.* **25**, 025005 (2012).
- [61] U. Patel, Y. Gao, D. Hover, G. J. Ribeill, S. Sendelbach, and R. McDermott, Coherent Josephson phase qubit with a single crystal silicon capacitor, *Appl. Phys. Lett.* **102**, 012602 (2013).